

Optimizing Electronic and Optical Responses of Novel Spin Transfer Torque-based Magnetic Tunnel Junctions with High Tunnel Magnetoresistance and Low Critical Currents

Tahereh Sadat Parvini,^{1,*} Elvira Paz,² Tim Böhner,^{2,†} Alejandro Schulman,² Luana Benetti,² Jakob Walowski,^{1,‡} Farshad Moradi,³ Ricardo Ferreira,² and Markus Münzenberg¹

¹*Institut für Physik, Universität Greifswald, Greifswald, Germany*

²*INL - International Iberian Nanotechnology Laboratory,
Avenida Mestre José Veiga, s/n, 4715-330 Braga, Portugal*

³*ICELab, Aarhus University, Denmark*

(Dated: March 23, 2023)

We developed and optimized two novel categories of spin transfer torque magnetic tunnel junctions (STT-MTJs), featuring a high tunnel magnetoresistance (TMR) ratio, low critical current, and out-oscillation behavior, which demonstrates their potential for low-power, high-speed, and reliable spintronic applications such as magnetic memory, logic, and signal processing. The SST-MTJs based on NiFe showed lower critical currents for auto-oscillation as compared to those based on CoFeSiB. Using VSM measurements that established comparable saturation magnetization and anisotropy field for both stacks, we attributed this observation to the higher damping of A-MTJs compared to B-MTJs. This hypothesis was verified through the all-optical time-resolved magneto-optical Kerr effect (TRMOKE) technique, which confirmed that STT-MTJs with lower damping exhibited auto-oscillation at lower critical current values. Beside, our study aimed to optimize the STT-MTJ performance, regarding the capping layer's impact on the device's response to electronic and optical stimuli.

The progress in deposition and crystal growth technologies has sparked significant interest in multilayer stacks, establishing them as a promising platform for advancing the fields of optical [1–3] and spintronic [4–6] devices. Magnetic tunnel junctions (MTJs), are multilayer structures consisting of two ferromagnetic layers separated by an insulating barrier, and exhibit multifaceted functionality and efficacy across a broad range of scientific domains, including data storage, sensing, and computing [7–11]. Spin-transfer torque-based magnetic tunnel junctions (STT-MTJs) represent the next generation of MTJs, employing the spin-transfer torque effect to control the magnetization of a ferromagnetic layer. Compared to conventional MTJs, STT-MTJs offer superior performance characteristics, including higher speed, lower power consumption, and greater scalability. With the emergence of STT-MTJs, the potential of these devices has been significantly expanded, opening up new possibilities for their use in a wide range of applications [12–20]. The critical current density (J_c) in STT-MTJs refers to the minimum current density required to generate sufficient spin-transfer torque to switch the magnetization of the free layer. It is a key parameter in determining the performance and reliability of STT-MTJs, as it directly affects the switching speed and energy efficiency of the device [21–25]. Since J_c is proportional to the magnetic damping constant of SST-MTJs, materials and stacks with a low damping are desired for high-speed and low-power spintronic devices.

In this study we developed two new types of in-plane magnetized SST-MTJs, which were optimized in terms of layer arrangement, thicknesses, and size of the MTJ

pillar to achieve a high TMR ratio and exhibit Vortex-based spin-torque nano-oscillator (STNO)-like behavior with low power consumption, i.e., a low critical current. The magnetization dynamics of the optimized SST-MTJs were scrutinized using time-resolved magneto-optical Kerr effect (TRMOKE) technique to extract key parameters, such as the damping coefficient and precession frequency.

Analysis of STT-MTJ Stacks: Structural Characterization and Electronic Response

A series of three distinct types of magnetic tunnel junctions (MTJs) were fabricated on SiO_2 (200nm) substrate using a singulus magnetron sputtering. As schematically depicted in Fig. 1(a), the MTJs were comprised of the following layers: 5 Ta / 50 CuN / 5 Ta / 50 CuN / 5 Ta / 5 Ru / 6 IrMn / 2 CoFe₃₀ / 0.825 Ru / 2.6 CoFe₄₀B₂₀ / MgO / Free Layer / Capping Layer, with thicknesses specified in nanometers. The free layer, which was the differentiating component among the MTJs, consists of 2 CoFe₄₀B₂₀ / X, where for type A-MTJ X≡0.21 Ta / 6 Co₆₇Fe₄Si_{14.5}B_{14.5}, for type B-MTJ X≡0.21 Ta / 7 Ni₈₀Fe₂₀ and for type C-MTJ X≡0. The thicknesses of CoFeSiB and NiFe in the A-MTJs and B-MTJs were meticulously chosen to guarantee comparable magnetic moments in both MTJs. The selection of Permalloy (NiFe) as the top magnetic layer in B-MTJs is based on its low crystalline anisotropy, which allows for easy magnetization switching with an external magnetic field. CoFeSiB-based MTJs (A-MTJs) demonstrate

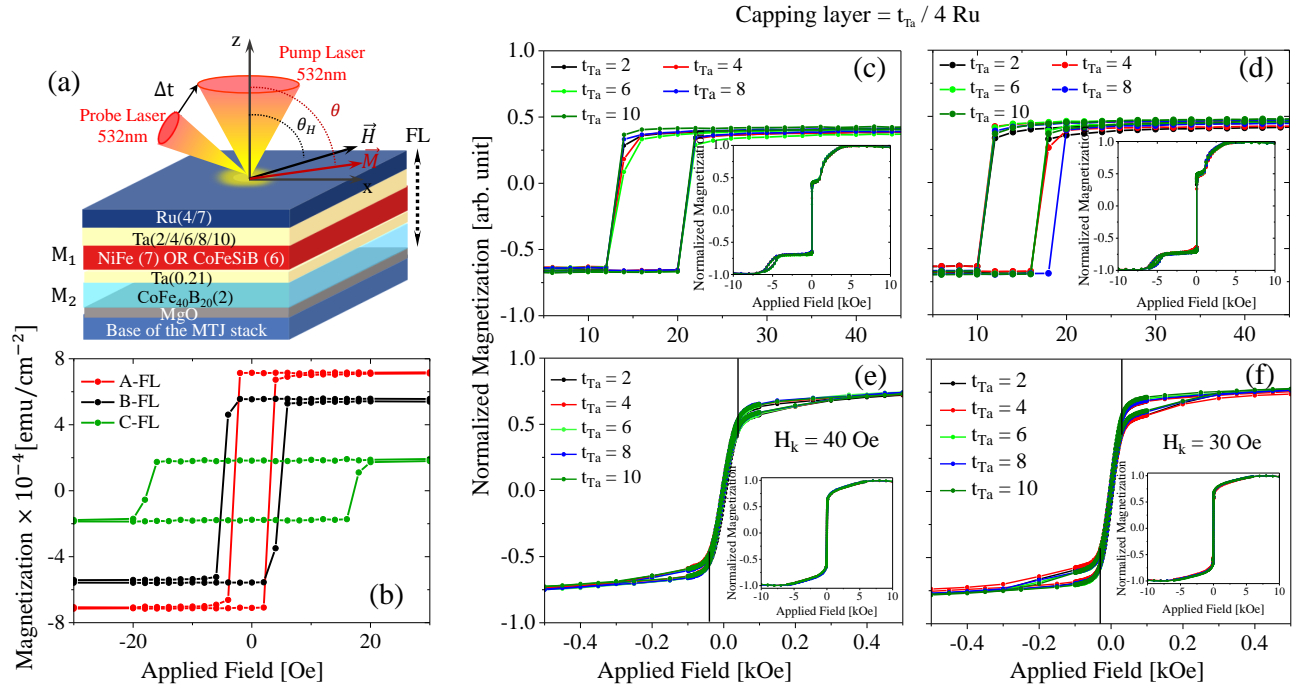


FIG. 1. (a) The illustration of the layer structure of optimized MTJs, with layer thicknesses indicated in nanometers, along with the geometry of ultrafast TRMOKE measurements. FL, \vec{H} , and \vec{M} indicate the free layer of the MTJ, external applied magnetic field, and magnetization vector of the stack. (b) Hysteresis loops of the free layer stacks along the easy axis of magnetization. (c) and(d) Hysteresis loops along the easy-axis for full stacks B-MTJ and A-MTJ, respectively, and along the hard-axis for B-MTJ and A-MTJ in (e) and (f), respectively. The influence of varying thicknesses of the capping layer Ta $t_{Ta} = 2/4/6/8/10$ nm on the anisotropy field and hysteresis response has been studied. The value of t_{Ru} is consistently 4nm across all of the plots.

improved MR ratios due to the absence of electron scattering caused by grain boundaries in their amorphous structure. Furthermore, the lack of crystallographic axes and grain boundaries enhances their thermal stability, rendering them an excellent choice for high-temperature MTJ applications. Three alternatives were considered for the fabrication of the capping layer, namely Ta/Ru, Cu/Ru, and Ra/Ru. The elements Ta, Cu, and Ru are employed to inhibit the crystallization of the adjacent magnetic layer, while a few nanometers of Ru on top of the MTJ are utilized for the passivation of the stacks. For achieving maximum performance in MTJs, characterized by high TMR, low critical current, and sustained thermal and electrical stability, the optimization of both the material and thickness of the capping layer are crucial. To achieve this goal, we fabricated a series of A-MTJ and B-MTJ stacks with distinct capping layers and varied thicknesses. The analysis of Fig. 1 and Fig. 1 SM [26], measured by a MicroSense EV9 vibrating sample magnetometer (VSM), demonstrates that the magnetic response of MTJs remains mostly unaffected by the modification of the capping layer material. Furthermore, The hysteresis response of the stacks remains unaffected by the variation in thickness of Ta adjacent to the top magnetic layer in capping layers. Table I displays the saturation magnetization values (M_s) of the distinct materials incorporated in the stack structures, namely CoFeSiB, CoFB, NiFe, and CoFeB, as determined by VSM measurements. These values are needed to accurately analyze the magnetization dynamics of the MTJs in the last section of our work.

tion magnetization values (M_s) of the distinct materials incorporated in the stack structures, namely CoFeSiB, CoFB, NiFe, and CoFeB, as determined by VSM measurements. These values are needed to accurately analyze the magnetization dynamics of the MTJs in the last section of our work.

TABLE I. Saturation magnetization M_s , in 10^3 A/m, of the materials: CoFe, CoFeB, NiFe, and CoFeSiB, measured by VSM.

Layer	CoFe ₃₀	CoFe ₄₀ B ₂₀	Ni ₈₀ Fe ₂₀	Co ₆₇ Fe ₄ Si _{14.5} B _{14.5}
M_s	1111.04	1358.98	680.61	1071.8

Furthermore, we synthesized simplified free layer stacks consisting of 5 Ta / 5 Ru / MgO / 2 CoFe₄₀B₂₀ / X / 2 Ta / 4 Ru, where X is defined as

- 0.21 Ta / 6 CoFe₄₀SiB₂₀ for A-FL,
- 0.21 Ta / 7 Ni₈₀Fe₂₀ for B-FL,
- and n/a for C-FL.

These fabricated FL stacks facilitated a comparative investigation of their magnetization dynamics responses

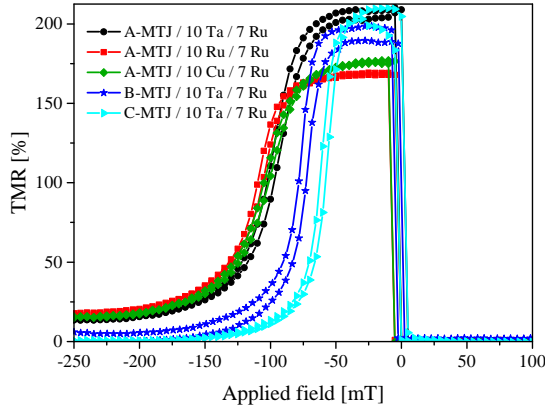


FIG. 2. (a) TMR ratios of A-MTJ, B-MTJ, and C-MTJ with capping layers of various heavy metals measured using CIPT as a function of the applied magnetic field.

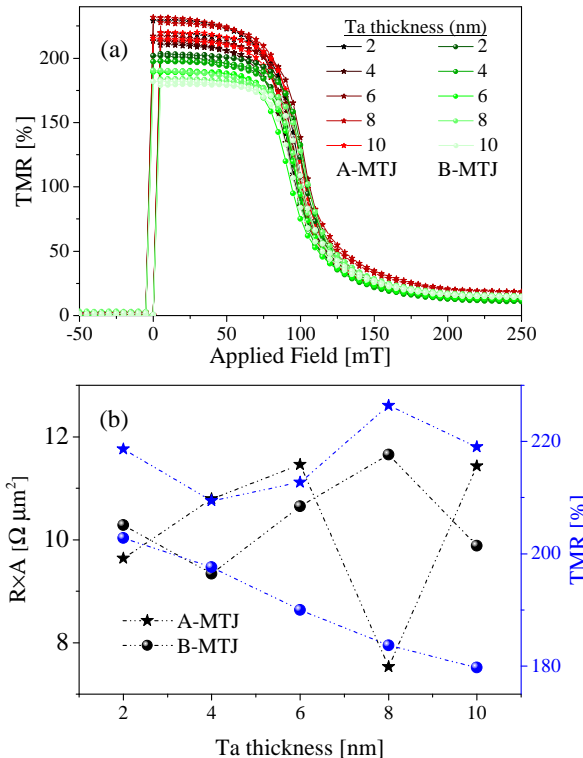


FIG. 3. (a) TMR Ratio of MTJs versus Ta capping layer with capping layer X Ta/ 7 Ru. (b) Variation of TMR values and resistance area with Ta thickness. The dashed-dotted lines are guides to the eyes.

with their corresponding full stacks. As depicted in Figure 1(b), incorporating a low anisotropy NiFe layer results in nearly a 50% decrease in the coercivity of the free layer, which can be further reduced by replacing NiFe with an amorphous CoFeSiB layer.

The application of a direct electrical current in MTJs generates spin-transfer torques (STTs) that facilitate the transfer of angular momentum from the stationary po-

larizing magnetic layer to the free magnetic layer. This transfer results in oscillatory magnetization dynamics, which in turn produce an oscillatory electrical response via the magnetoresistance effect. The difference in resistance between parallel (R_{AP}) and antiparallel (R_P) magnetization configurations can be normalized to obtain the tunnel magnetoresistance ratio (TMR), expressed as $TMR = \frac{R_{AP} - R_P}{R_P}$. The electrical properties of STT-MTJs were characterized using Current-In-Plane Tunneling (CIPT) measurements, and the resulting transfer curves for various stacks are presented in Figure 2. The TMR ratio of the B-MTJ stack is lower compared to the A-MTJs and resembles that of the control stack, C-MTJ. Our findings prove that the use of Ta in the capping layer of an MTJ stack leads to a higher TMR ratio compared to stacks utilizing Ru or Cu capping layers. We attribute this observation to the improved interface quality in stacks with Ta in the capping layer which enhances spin-dependent transport. In contrast, Ru and Cu are prone to oxidation, which can lead to the formation of unwanted oxide layers and negatively impact the TMR performance [27, 28]. The exact measured values of the TMR ratio and resistance area ($R \times A$) of the aforementioned stacks are reported in Table II. In these STT-MTJs, the thickness of the MgO tunnel barrier is precisely selected to obtain a resistance area of approximately $10 \Omega(\mu\text{m})^2$, which has been experimentally established as the optimal range for attaining maximum output power.

TABLE II. The TMR ratio and resistance-area values obtained from CIPT measurements for three different types of SST-MTJs.

MTJ Stacks	TMR (%)	$R \times A (\Omega\mu\text{m}^2)$
B-MTJ / 10 Ta / 7 Ru	190	11.2
A-MTJ / 10 Ta / 7 Ru	208	9.6
A-MTJ / 10 Ru / 7 Ru	168	10.3
A-MTJ / 10 Cu / 7 Ru	179	11.0
C-MTJ / 10 Ta / 7 Ru	199	11.9

Having proven the superior performance of MTJs with the Ta capping layer, we embarked on an effort to determine the optimal thickness of the Ta layer for maximizing SST-MTJs' performance. As a consequence, we fabricate a collection of A-MTJs and B-MTJs, each with distinct thicknesses of Ta, namely $t_{Ta}=2/4/6/8/10$ nm and a constant thickness of $t_{Ru}=7$ nm. The TMR ratio and resistance area of these stacks are shown in Fig. 3 (a) and (b). The TMR ratio of the B-MTJs exhibited a decrease as the thickness of Ta increased, whereas no noteworthy change in the TMR ratio of the A-MTJs was observed. Two potential reasons for the observed effect

of Ta capping layer thickness on the TMR ratio are its role as a Boron sink, which is known to affect the TMR ratio through Boron diffusion, and its potential influence on the crystallization of the free layer. The crystallization of Ta depends on its thickness, with thin layers (<5 nm) crystallizing in beta-phase and thicker layers (>10 nm) in alpha-phase, which could affect the overall crystallization of the stack. However, the 0.21 nm Ta layer in the free layer is specifically designed to mitigate the influence of NiFe crystallization on CoFeB, which ultimately determines the TMR ratio.

The minimum current density required to trigger the STT oscillations in the MTJs is critical current density, J_c . For B-MTJ with a diameter of 300 nm critical current is about 3mA, or on the other hand around 0.04 A/ μ m 2 , whereas no auto-oscillation was observed at low critical currents in the A-MTJs. To theoretically validate these observations, we utilized the macrospin model, which provides an expression for critical current as [29–31]

$$J_c = \frac{2e\mu_0 M_s \alpha d}{\hbar} \left[\frac{M_s}{2} + H + H_k \right] \cdot \frac{1}{P}, \quad (1)$$

where e is the charge of the electron, μ_0 is the permeability of free space, \hbar the Planck constant, M_s the magnetization saturation, α the Gilbert damping constant, d the thickness of the free layer, and P the spin polarization. As previously described, both the B-MTJs and A-MTJs possess comparable saturation magnetization and anisotropy; thus, the relatively lower critical current of the former as compared to the latter can be attributed to their reduced damping. To validate this hypothesis, we utilized an TRMOKE technique method to measure the damping of the stacks. The MTJs with Ru and Cu capping layers not only demonstrated inferior performance when compared to those with a Ta capping layer, but also produced a noisier Kerr signal in TRMOKE measurements due to their elevated laser absorption and subsequently decreased penetration depth (under the same power of laser and magnetic field). Therefore in the following, only MTJs with capping layer X Ta/4 Ru are reported, due to their higher signal to noise ratio in the TRMOKE measurements.

Investigating the Magnetization Dynamics of the optimized SST-MTJs

We employed an all-optical approach to investigate magnetization dynamics of the optimized SST-MTJs using femtosecond (fs) laser pulses in a pump-probe configuration (see Fig. 1 (a)). The pump and probe pulses had central wavelengths of ~ 800 nm, pulse durations of 40 fs, and repetition rates of 250 kHz. The pump and probe spot radii were 110 μ m and 30 μ m, respectively.

Ultrafast demagnetization was induced by pump laser illumination, resulting in magnetization recovery and the damped precession of magnetization observed after a delay time of a few hundred femtoseconds. The static polar Kerr rotation angle θ_k was measured using the probe laser pulse. All TRMOKE measurements were performed at room temperature under an external magnetic field of up to 0.15 T at a fixed angle of $\theta_H = 75^\circ$ measured from the film normal. The Supplementary Materials (SM) [26] contains documentation on the magnetization precession of free layer stacks and optimized full SST-MTJ stacks with varying capping layer thicknesses. The Fourier spectrum analysis of Kerr's data, as reported in [26], reveals a single dominant precession frequency in all SST-MTJ, attributed to the direct ferromagnetic coupling of M_1 and M_2 through ultra-thin Ta layer and consequently their collective precession. Consequently, the macrospin model was utilized to derive the fitting function, enabling the determination of effective damping and precession frequency, and to solve the Landau–Lifshitz–Gilbert (LLG) equation, facilitating the determination of intrinsic damping in the MTJs. Then, TMOKE signals underwent a fitting process utilizing a damped-harmonic function with an exponential decay background and a sinusoidal term to achieve a meticulous analysis of the magnetization dynamics in stacks [32–34](detail in SM). Utilizing the applied fitting model, the precession frequencies (f) and magnetization relaxation times (τ) corresponding to each SST-MTJS's macrospin were extracted. Fig. 4 (a) and (c) reveals that the precession frequency of the macrospin in each stack is positively correlated with the magnetic field strength, with no noticeable impact from the thickness of the capping layer. Furthermore, the frequency of the full stack is lower than that of free layers, attributed to interlayer couplings. This interaction induces a shift in magnetic anisotropy and promotes a more stable configuration of magnetic moments, resulting in a reduction of the precession frequency. The effective damping coefficient of the macrospin vector denoted as α_{eff} and calculated using the formula $\alpha_{eff} = (2\pi f\tau)^{-1}$, is a measure of the total damping, encompassing both intrinsic Gilbert damping (α_0) and extrinsic damping mechanisms. Under high fields, it suppresses extrinsic contributions and approaches the intrinsic Gilbert damping parameter, sees Fig. 4 (b) and (d). The complexity of magnetization behavior and the greater contribution of inhomogeneous broadening make data collected at low magnetic fields particularly challenging to interpret. Therefore, to obtain a clearer understanding of the magnetization dynamics, high-field data is preferred. Overall, this figure indicates that B-MTJs exhibit both higher frequency and lower damping when compared to A-MTJs. The higher damping coefficient of A-MTJs compared to B-MTJs can be attributed to a combination of factors including its electronic structure with strong spin-orbit coupling due to the presence of heavy elements, lower

magnetic anisotropy, and fine-grained and amorphous microstructure of CoFeSiB.

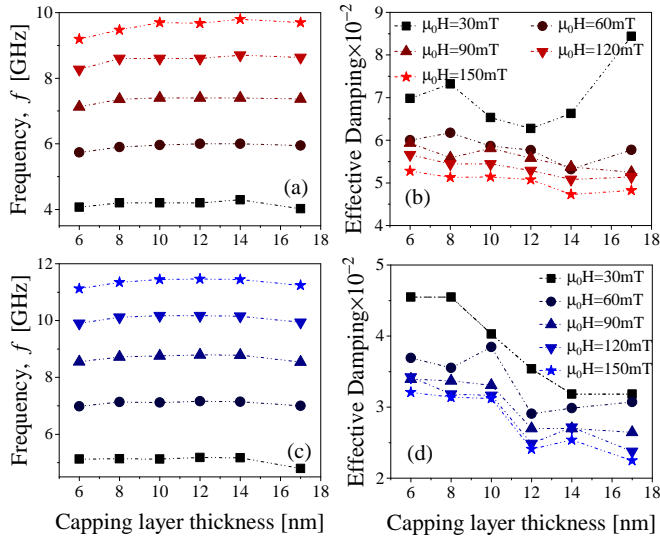


FIG. 4. The precession frequency and effective damping constant α_{eff} as a function of capping layer thickness ($t_{Ta} + t_{Ru}$) for A-MTJs ((a) and (b)) and B-MTJs ((c) and (d)). The power of the pump is set to a constant value of 300 mW, while magnetic fields of 30, 60, 90, 120, and 150 mT (25° out of plane) are applied.

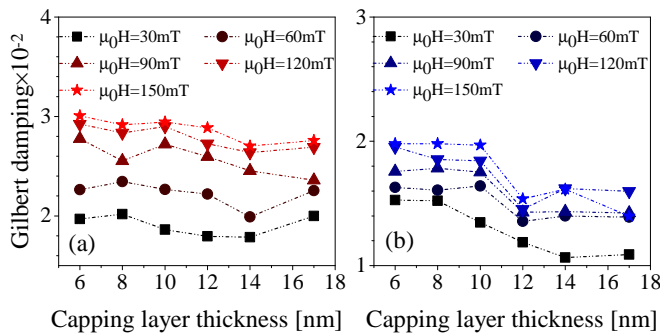


FIG. 5. Intrinsic Gilbert damping constant of (a) A-MTJ and (b) B-MTJ stacks as a function of the total capping layer thickness, $t_{Ta} + t_{Ru}$.

To extract the intrinsic Gilbert damping parameter using Gilbert's ansatz, it is essential to establish a connection between the exponential decay time τ and α_0 . Assuming negligible in-plane anisotropy and small tilting angles of the magnetization out of the sample plane ($\theta \approx \frac{\pi}{2}$), the precession frequency can be derived using Kit-

tel's formula $\omega = \gamma \sqrt{\mu_0 H_x} \left[\mu_0 H_x + \mu_0 M_s - \frac{2K_z}{M_s} \right]$ where ω is the angular frequency of the precession, $\gamma = \frac{g\mu_B}{\hbar}$ is the gyromagnetic ratio of MTJ stacks, μ_0 and μ_B are the vacuum permeability and Bohr magneton respectively, g is the Landé g-factor, and $H_k = 2K_z/M_s$ is the perpendicular anisotropy field [35–38]. By using the M_s and H_k

data acquired from the VSM and utilizing a curve-fitting algorithm to match Kittel's formula with the corresponding frequencies derived from the TRMOKE, it is possible to determine the γ (reported in Fig. 8(SM) [26]). Subsequently, the intrinsic Gilbert damping constant can be determined using the following equation:

$$\alpha_0 = \left[\frac{\tau\gamma}{2} \left(2\mu_0 H_x + \mu_0 M_s - \frac{2K_z}{M_s} \right) \right]^{-1}. \quad (2)$$

In the high-field limit, neglecting the anisotropy contribution yields an approximation of $\alpha_0 = (2\pi f\tau)^{-1}$. The intrinsic Gilbert damping of stacks with different capping layers are shown in Fig. 5. This observation clearly illustrates the convergence of effective and intrinsic damping at high magnetic fields. Additionally, this observation confirms that B-MTJs exhibit lower intrinsic damping than A-MTJs, which correlates with the lower critical current density of B-MTJs. Consistent with the TMR ratio measurements, the A-MTJ stacks exhibit lower sensitivity to changes in capping layer thickness compared to the B-MTJ stacks, with negligible alteration in damping observed across varying thicknesses.

CONCLUSION

Through rigorous structural and dimensional optimization, we meticulously engineered two distinct magnetic tunnel junction stacks, ultimately achieving a remarkable combination of high TMR ratio and low critical current for auto-oscillation. The sole point of differentiation between MTJs lies within the free layer composition, where category A-MTJs utilize 2 CoFeB / 0.21 Ta / 6 CoFeSiB, and category B-MTJs incorporate 2 CoFeB / 0.21 Ta / 7 NiFe. Incorporating CoFeSiB as the top magnetic layer resulted in a high TMR of approximately $\simeq 208\%$, while stacks containing NiFe exhibited 15–20 percent lower TMR. Moreover, the critical current, which represents the minimum current necessary to induce a magnetic state transition, is relatively lower for B-MTJs compared to A-MTJs. The nearly identical saturation magnetization and anisotropy field values measured by VSM led to the conclusion that the lower critical current measured in B-MTJs could be attributed to lower damping. To validate this hypothesis, we employed the all-optical TRMOKE technique and demonstrated that the damping exhibited by the B-MTJs was approximately half that of the A-MTJs.

ACKNOWLEDGEMENT

This project has received funding from the European Union's Horizon 2020 research and innovation program under grant agreement No 899559 (SpinAge).

* tahereh.parvini@uni-greifswald.de
 † tim.bohnert@inl.int
 ‡ jakob.walowski@uni-greifswald.de

[1] P. A. Pantazopoulos and N. Stefanou, *Phys. Rev. B* **99**, 144415 (2019).

[2] H. Yu, J. Xiao, and H. Schultheiss, *Phys. Rep.* **905**, 1 (2021).

[3] T. Parvini, M. Tehranchi, and S. Hamidi, *Appl. Phys. A* **118**, 1447 (2015).

[4] T. Endoh and H. Honjo, *Journal of Low Power Electronics and Applications* **8**, 44 (2018).

[5] A. Tanwear, X. Liang, Y. Liu, A. Vuckovic, R. Ghanam, T. Böhnert, E. Paz, P. P. Freitas, R. Ferreira, and H. Heidari, *IEEE Transactions on Biomedical Circuits and Systems* **14**, 1299 (2020).

[6] F.-F. Stiewe, T. Winkel, Y. Sasaki, T. Tubandt, T. Kleinke, C. Denker, U. Martens, N. Meyer, T. S. Parvini, S. Mizukami, *et al.*, *Appl. Phys. Lett.* **120**, 032406 (2022).

[7] J.-G. J. Zhu and C. Park, *Mater. Today* **9**, 36 (2006).

[8] M. Tarequzzaman, A. Jenkins, T. Böhnert, J. Borme, L. Martins, E. Paz, R. Ferreira, and P. Freitas, *Appl. Phys. Lett.* **112**, 252401 (2018).

[9] H. Yang, X. Hu, S. Sievers, T. Boehnert, M. Tarequzzaman, J. Costa, R. Ferreira, M. Bieler, and H. Schumacher, *J. Appl. Phys.* **124**, 174501 (2018).

[10] N. Maciel, E. Marques, L. Naviner, Y. Zhou, and H. Cai, *Sensors* **20**, 121 (2019).

[11] N. Jha, A. Pariyar, T. S. Parvini, C. Denker, P. K. Vardhanapu, G. Vijaykumar, A. Ahrens, T. Meyer, M. Seibt, N. Atodiresei, *et al.*, *ACS Appl. Electron. Mater.* (2022), 10.1021/acsaelm.2c01428.

[12] S. S. Parkin, M. Hayashi, and L. Thomas, *Science* **320**, 190 (2008).

[13] S. Ikeda, J. Hayakawa, Y. M. Lee, F. Matsukura, Y. Ohno, T. Hanyu, and H. Ohno, *IEEE Trans. Electron Devices* **54**, 991 (2007).

[14] Z. Jin, T. M. Koo, M. S. Kim, M. Al-Mahdawi, M. Oogane, Y. Ando, and Y. K. Kim, *AIP Adv.* **11**, 015046 (2021).

[15] X. Liu, C. Ren, and G. Xiao, *J. Appl. Phys.* **92**, 4722 (2002).

[16] L. Wang, H. Cheng, P. Li, Y. L. van Hees, Y. Liu, K. Cao, R. Lavrijsen, X. Lin, B. Koopmans, and W. Zhao, *Proceedings of the National Academy of Sciences* **119**, e2204732119 (2022).

[17] S. Peng, Y. Zhang, M. Wang, Y. Zhang, and W. Zhao, *Wiley Encyclopedia of Electrical and Electronics Engineering*, 1 (1999).

[18] J. Z. Sun, *Phys. Rev. B* **62**, 570 (2000).

[19] X. Fong, Y. Kim, R. Venkatesan, S. H. Choday, A. Raghunathan, and K. Roy, *Proceedings of the IEEE* **104**, 1449 (2016).

[20] H. Farkhani, T. Böhnert, M. Tarequzzaman, J. D. Costa, A. Jenkins, R. Ferreira, J. K. Madsen, and F. Moradi, *Frontiers in neuroscience* **13**, 1429 (2020).

[21] S. Verma, S. Kaundal, and B. K. Kaushik, *IEEE Trans. Magn.* **50**, 1 (2014).

[22] Z. Diao, Z. Li, S. Wang, Y. Ding, A. Panchula, E. Chen, L.-C. Wang, and Y. Huai, *J. Phys. Condens. Matter* **19**, 165209 (2007).

[23] K. C. Chun, H. Zhao, J. D. Harms, T.-H. Kim, J.-P. Wang, and C. H. Kim, *IEEE J. Solid-State Circuits* **48**, 598 (2012).

[24] B. Koopmans, J. Ruigrok, F. Dalla Longa, and W. De Jonge, *Phys. Rev. Lett.* **95**, 267207 (2005).

[25] D. Huang, D. Lattery, and X. Wang, *ACS Appl. Electron. Mater.* **3**, 119 (2020).

[26] Supplemental Material at [URL will be inserted by publisher] for [give brief description of material].

[27] T. Nagahama, S. Yuasa, E. Tamura, and Y. Suzuki, *Phys. Rev. Lett.* **95**, 086602 (2005).

[28] K. Tsumekawa, D. Djayaprawira, M. Nagai, H. Maehara, S. Yamagata, and N. Watanabe, in *2005 IEEE International Magnetics Conference (INTERMAG)* (2005) pp. 1983–1984.

[29] G. Khalsa, M. D. Stiles, and J. Grollier, *Appl. Phys. Lett.* **106**, 242402 (2015).

[30] J. Costa, S. Serrano-Guisan, B. Lacoste, A. Jenkins, T. Böhnert, M. Tarequzzaman, J. Borme, F. Deepak, E. Paz, J. Ventura, *et al.*, *Sci. Rep.* **7**, 1 (2017).

[31] L.-B. Faber, W. Zhao, J.-O. Klein, T. Devolder, and C. Chappert, in *2009 4th International Conference on Design & Technology of Integrated Systems in Nanoscale Era* (IEEE, 2009) pp. 130–135.

[32] G.-M. Choi, J. H. Oh, D.-K. Lee, S.-W. Lee, K. W. Kim, M. Lim, B.-C. Min, K.-J. Lee, and H.-W. Lee, *Nat. Commun.* **11**, 1 (2020).

[33] G.-M. Choi, B.-C. Min, K.-J. Lee, and D. G. Cahill, *Nat. Commun.* **5**, 1 (2014).

[34] C. Gonçalves, A. Silva, D. Navas, M. Miranda, F. Silva, H. Crespo, and D. Schmool, *Sci. Rep.* **6**, 1 (2016).

[35] B. Khodadadi, J. B. Mohammadi, J. M. Jones, A. Srivastava, C. Mewes, T. Mewes, and C. Kaiser, *Phys. Rev. Appl.* **8**, 014024 (2017).

[36] Y. Zhang, G. Wu, Z. Ji, X. Chen, Q. Jin, and Z. Zhang, *Phys. Rev. Appl.* **17**, 034033 (2022).

[37] W. Wang, P. Li, C. Cao, F. Liu, R. Tang, G. Chai, and C. Jiang, *Appl. Phys. Lett.* **113**, 042401 (2018).

[38] J. Walowski, M. D. Kaufmann, B. Lenk, C. Hamann, J. McCord, and M. Münzenberg, *J. Phys. D: Appl. Phys.* **41**, 164016 (2008).

Optimizing Electronic and Optical Responses of Novel Spin Transfer Torque-based Magnetic Tunnel Junctions with High Tunnel Magnetoresistance and Low Critical Currents

Tahereh Sadat Parvini,^{1,*} Elvira Paz,² Tim Böhnert,^{2,†} Alejandro Schulman,² Luana Benetti,² Jakob Walowski,^{1,‡} Farshad Moradi,³ Ricardo Ferreira,² and Markus Münzenberg¹

¹*Institut für Physik, Universität Greifswald, Greifswald, Germany*

²*INL - International Iberian Nanotechnology Laboratory,
Avenida Mestre José Veiga, s/n, 4715-330 Braga, Portugal*

³*ICELab, Aarhus University, Denmark*

(Dated: March 23, 2023)

Hysteresis loop of the A-MTJs with different capping layer material

Fig. 1 shows the magnetic hysteresis loops of A-MTJs with different capping layers measured using a MicroSense EV9 vibrating sample magnetometer (VSM) with the magnetic field applied parallel and perpendicular to the easy axis. All three stacks show the same magnetic anisotropy field $H_k = 30\text{ Oe}$. The superior TMR ratio of MTJs incorporating Ta capping layers, in comparison to those with Cu and Ru capping layers, can be attributed to the Ta layer's capacity to enhance interfacial quality and promote a more uniform interface between the ferromagnetic and capping layers. This leads to a reduction in interfacial scattering and an enhancement in spin-dependent tunneling across the MTJ.

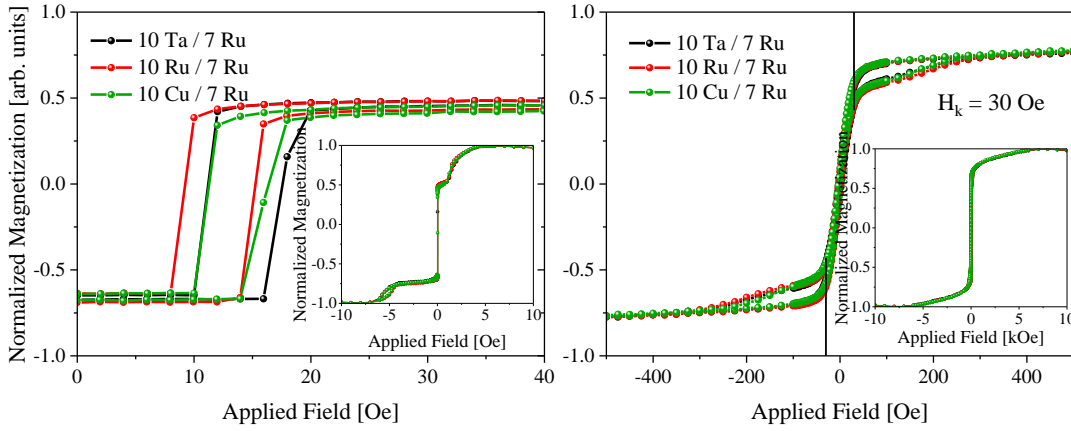


FIG. 1. (a) Easy axis and (b) hard axis VSM measurement of the magnetic moment per area of A-MTJ stacks with different capping layers.

Time-Resolved Magneto-Optic Kerr Effect (TRMOKE) Measurements

Time-resolved magneto-optical Kerr effect (TRMOKE) signals of the free layer (FL) simplified stacks, 5 Ta / 5 Ru / MgO / 2 CoFe₄₀B₂₀ / X / 2 Ta / 4 Ru with X≡0.21 Ta / 6 CoFe₄₀SiB₂₀ for A-FL stack and X≡0.21 Ta / 7 Ni₈₀Fe₂₀ for B-FL stack as a function of applied magnetic field amplitude are shown in Fig. 2 (b) and (a), respectively. In order to obtain a correct fit of the precessional processes, without any contamination from the ultrafast demagnetization, the TRMOKE measurements were fitted, after a delay time of 1 ps, to a damped-harmonic function superposed with an exponential decay background

$$\Delta\theta_k = A + Be^{-vt} + C\sin(2\pi ft + \phi_0)e^{-t/\tau}, \quad (1)$$

Here, the first two terms represent the change due to the recovery from the demagnetization and are characterized by the amplitudes of A and B and the recovery rate v . The last term represents the change due to the damped

magnetization precession. C , f , τ , and ϕ_0 denote the precession amplitude, frequency, lifetime, and initial phase, respectively. First, the TRMOKE data were fitted with Eq. 1 to extract the values of the precession frequencies (f) and magnetization relaxation times (τ). The precession frequency increases while the relaxation time decreases with a rise in the magnetic field, as illustrated in Fig. 2 (c). For every magnetic field value, the B-FL stack exhibits a frequency approximately one GHz higher than the A-FL stack. The intrinsic damping α_0 is an important parameter of stacks that has garnered significant attention. An alternative method for evaluating it involves determining the effective Gilbert damping parameter, $\alpha_{eff} = (2\pi f\tau)^{-1}$, which can be calculated using the fitted values of f and τ (refer to Fig. 2 (d)). The α_{eff} values under high fields suppress the extrinsic contributions such as the inhomogeneous anisotropy and thus approximately equals the intrinsic α_0 . However, in lower fields, α_{eff} is larger than α_0 . To obtain the Gilbert damping parameter intrinsic to the sample geometry (not intrinsic to the material), we fit Kittel's formula, with extracted frequencies and derive the gyromagnetic ratio of the stacks by treating that as a fit parameter after inputting the values of $4\pi M_s$, H_k extracted from VSM measurements, as shown in Fig. 2 (e). It is important to note that the middle Ta layer has an extremely low thickness of 0.2 nm, rendering it nothing more than an impurity. Additionally, the FFT spectrum depicting a single precession frequency has led us to conclude that the free layer, comprising two magnetic layers, behaves like a macrospin. For this reason, in the calculations we used $M_s^{B-FL} = \frac{t_{NiFe}M_s^{NiFe} + t_{CoFeB}M_s^{CoFeB}}{t_{NiFe} + t_{CoFeB}}$ and $M_s^{A-FL} = \frac{t_{CoFeSiB}M_s^{CoFeSiB} + t_{CoFeB}M_s^{CoFeB}}{t_{CoFeSiB} + t_{CoFeB}}$ as magnetization saturation of the B-FL and A-FL stacks respectively. The obtained values of intrinsic damping are shown in Fig. 2 (f). According to these experiments, we consider that the B-FL stack has the advantage of achieving low damping for STT switching.

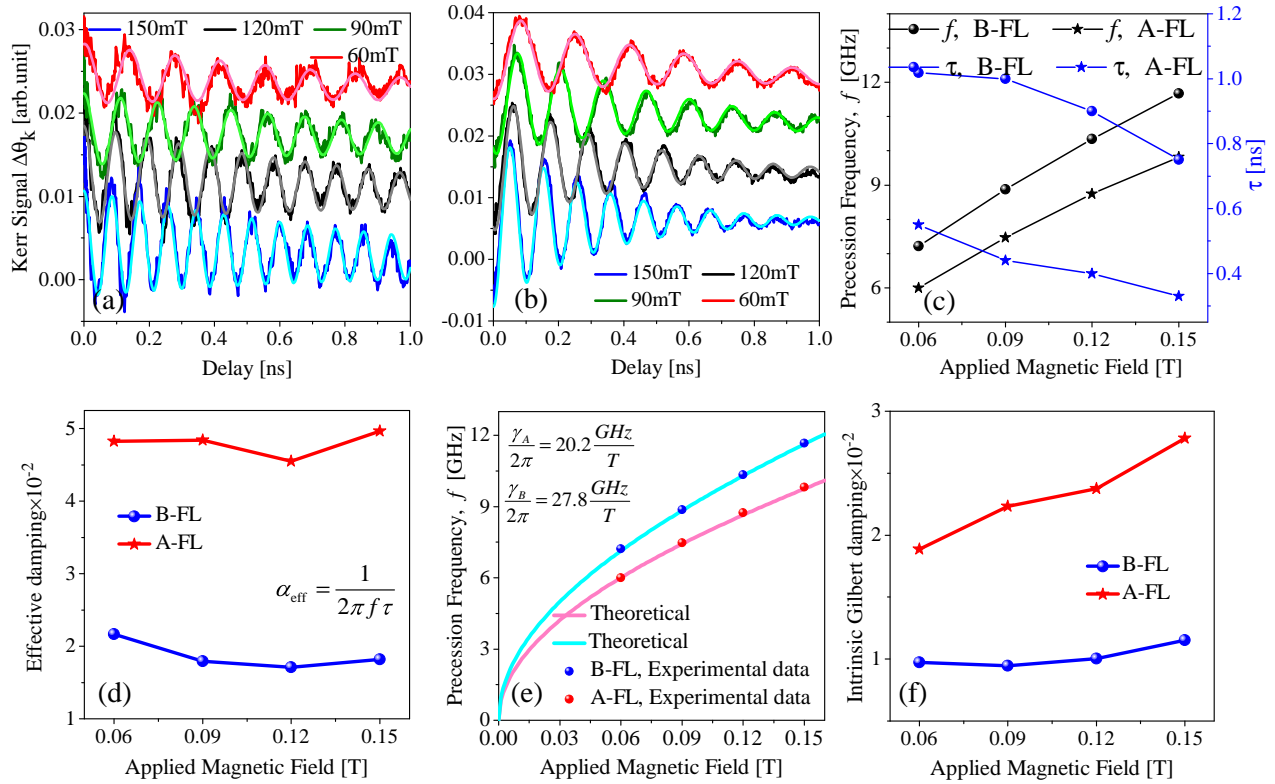


FIG. 2. Time-resolved magneto-optical Kerr effect (TRMOKE) signals measured at a pump laser power of 300mW for free layer stacks (a) B-FL and (b) A-FL under different external applied fields $\mu_0 H = 60, 90, 120$, and 150 mT (25° out of plane). Theoretical curves (solid curves) are fit to the experimental data (filled circles) using Eq. 1. (c) Precession frequency (f) and relaxation time (τ) obtained using the fitting function. The solid lines are guides to the eyes. (d) Effective damping coefficient as a function of the applied magnetic field. The solid lines are guides to the eyes. (e) Frequency as a function of magnetic field bias magnetic field. Symbols represent experimental data points and a solid curve is fitted to the Kittel formula. (f) Gilbert damping constant as a function of the applied magnetic field. The symbols represent experimental data points and the solid lines guide the eyes.

Following this, we investigated the magnetization dynamics of the full stacks of A-MTJs and B-MTJs with different capping layer thicknesses, denoted as $t_{Ta} + t_{Ru}$. TRMOKE signal of the B-MTJ and A-MTJ stacks measured at a pump laser power of 300mW by applying varying external magnetic fields $\mu_0 H = 60, 90, 120$, and 150 mT (25° out

of plane) are shown in Fig. 3 and 4 respectively. It can be seen that as the magnetic field strength increases, there is an increase in the precession frequency and a decrease in the relaxation time of the magnetization vector across all stacks. In both categories of MTJs, there is a consistent reduction in the M_s value observed as the thickness of the capping layer increases and the magnetic field amplitude decreases. The fast Fourier transform (FFT) of the TRMOKE data after subtracting the exponential background for A-MTJs and B-MTJs are respectively shown in Fig. 5 and Fig. 6. The energy dissipation process from electron spins to the lattice and subsequently to the surroundings during remagnetization, followed by ultrafast demagnetization, is a key contributing factor to the observed background effect. According to the FFT spectra, all stacks show a single precession frequency which is attributed to the collective precession of the magnetization vector in the first ferromagnetic layer (CoFe₄₀SiB₂₀ (6 nm) or Ni₈₀Fe₂₀ (7 nm)) and second ferromagnetic layer (CoFe₄₀B₂₀) within the free layers. The study's results suggest that the entire stack can be modeled as a macrospin, allowing for the use of the Landau-Lifshitz-Gilbert (LLG) equation with a macrospin model. This enables the accurate determination of frequency and damping parameters. The observed shift in the frequency of the uniform precessional mode towards lower values, as the bias magnetic field is reduced, provides evidence of the magnetic nature of the modes. The experimental results reveal that the precession frequency of the samples remains unchanged upon increasing the thickness of the capping layers. In comparison to A-MTJ stacks, B-MTJs exhibit a higher precession frequency and reduced oscillation amplitude attributed to the smaller saturation magnetization of NiFe compared to CoFeSiB. Additionally, B-MTJs demonstrate lower effective damping than A-MTJs. The α_{eff} values under high fields suppress the extrinsic contributions such as the inhomogeneous anisotropy and thus approximately equals the intrinsic α_0 . The gyromagnetic ratio values for A-MTJs and B-MTJs, as presented in Fig. 7, were obtained using a method akin to that employed for free layers. Similarly, the full stacks containing NiFe exhibit a higher gyromagnetic ratio compared to those containing CoFeSiB.

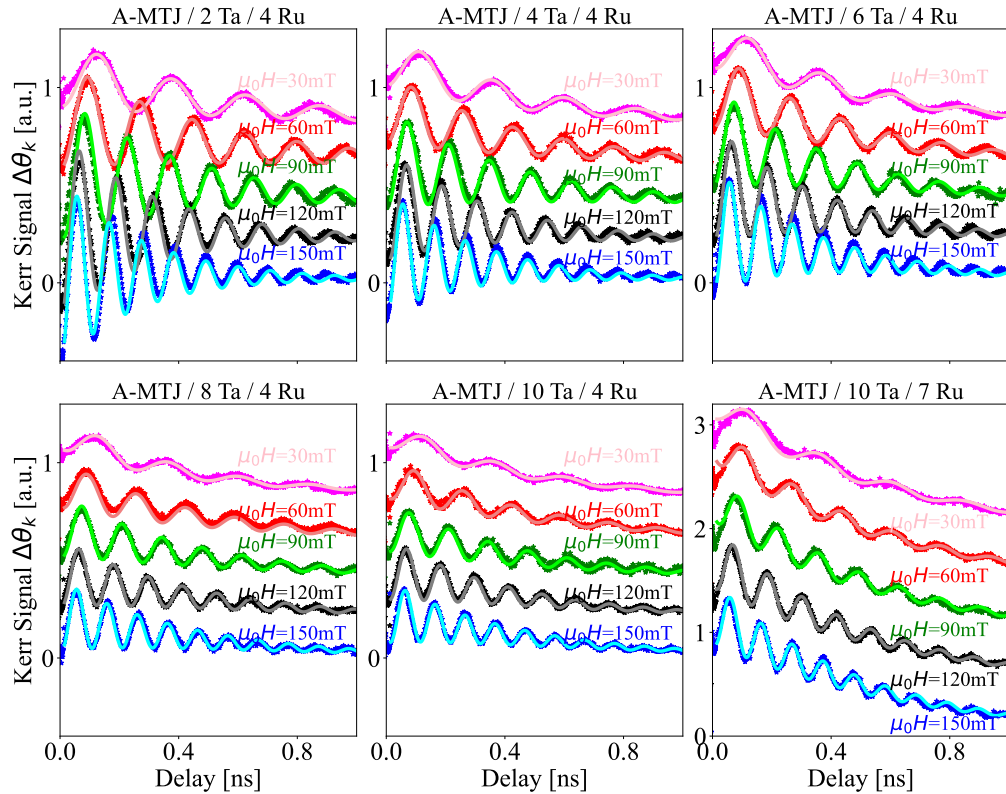


FIG. 3. Kerr rotation spectra for A-MTJs, measured for fields applied for 30, 60, 90, 120, and 150 mT (25° out of plane). Curves acquired by fitting function and experimental results are shown by solid lines and star points respectively.

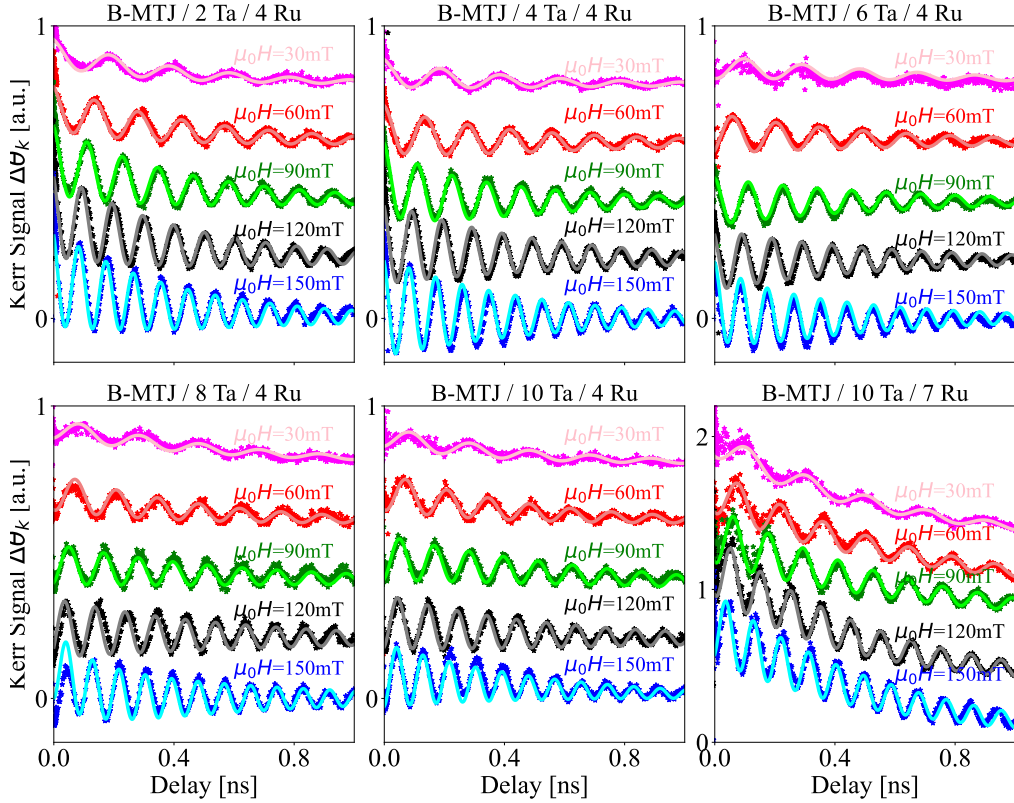


FIG. 4. Kerr rotation spectra for B-MTJs, measured for fields applied for 30, 60, 90, 120, and 150 mT (25° out of plane). Curves acquired by fitting function and experimental results are shown by solid lines and star points respectively.

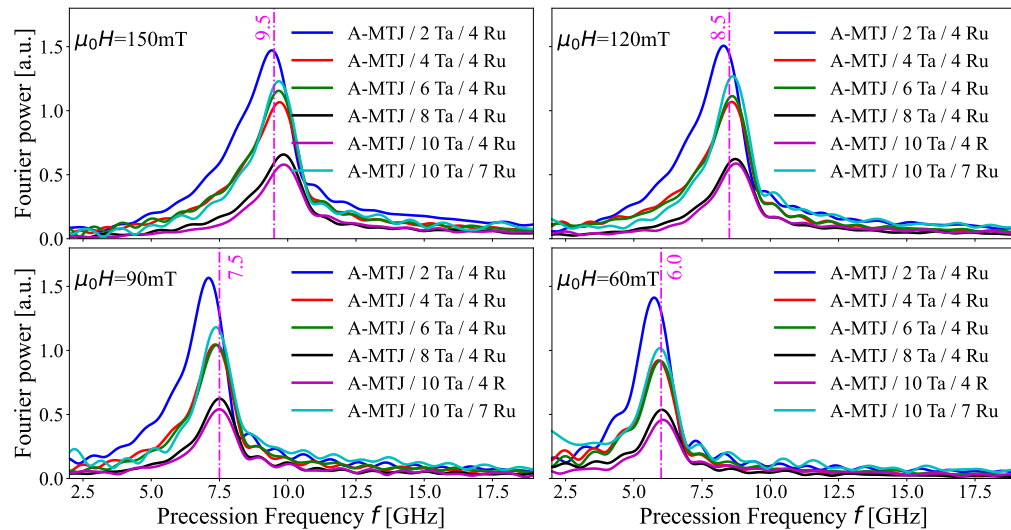


FIG. 5. Fourier power spectra of A-MTJs with different thicknesses of the capping layer, measured for fields applied for 30, 60, 90, 120, and 150 mT (25° out of plane).

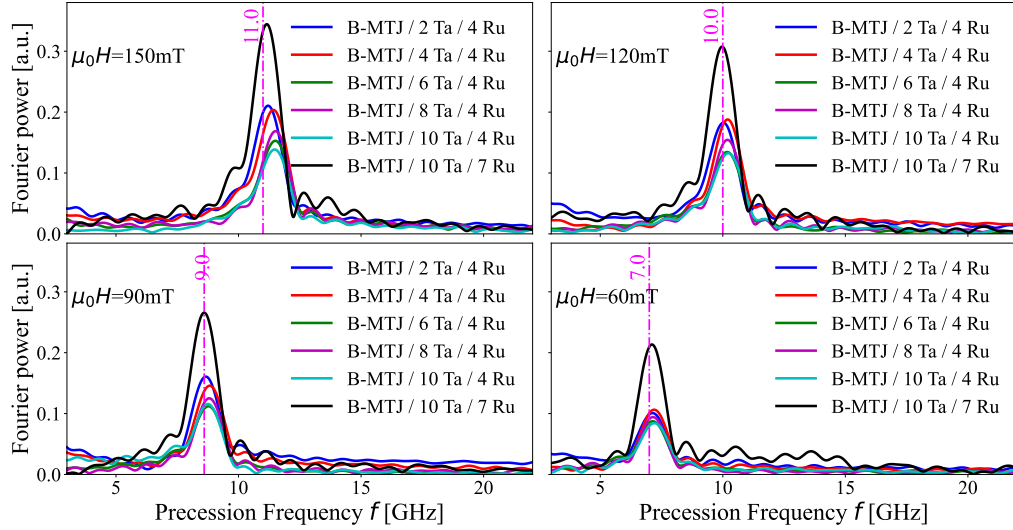


FIG. 6. Fourier power spectra of B-MTJs with different thicknesses of the capping layer, measured for fields applied for 30, 60, 90, 120, and 150 mT (25° out of plane).

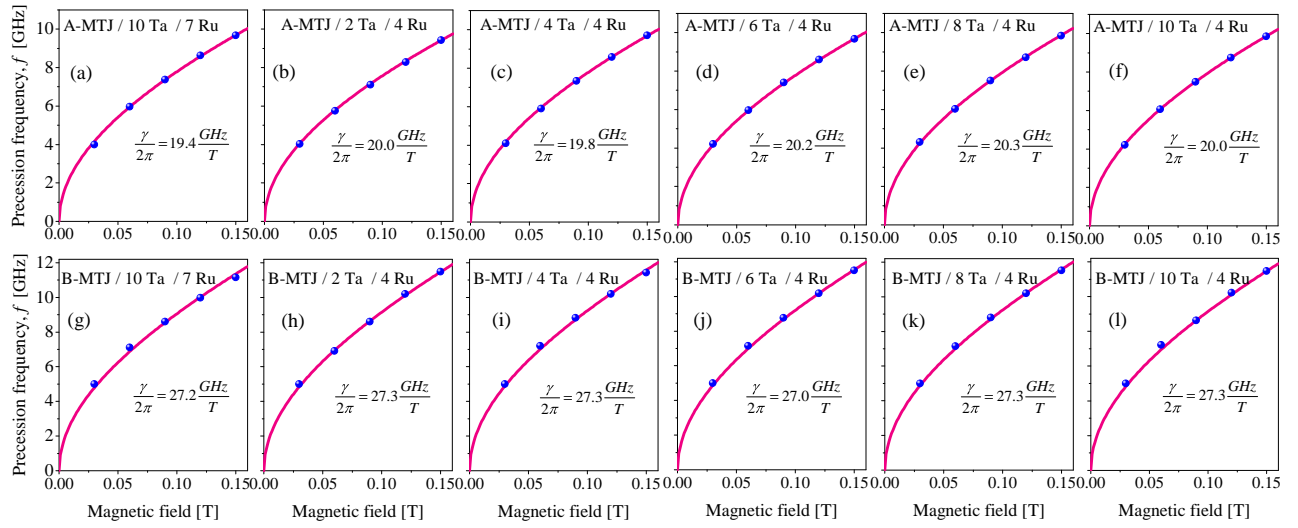


FIG. 7. Frequency as a function of magnetic field bias magnetic field. Symbols represent experimental data points and a solid curve is fitted to the Kittel formula.